A Generalized van't Hoff Relation for the Temperature Dependence of Complex-valued Nonlinear Spectra

Ashley K. Borkowski, Hasini S. Senanayake, and Ward H. Thompson^{a)}
Department of Chemistry, University of Kansas, Lawrence, KS 66045, USA

(Dated: 9 July 2024)

The temperature dependence of spectra can reveal important insights into the structural and dynamical behavior of the system being probed. In the case of linear spectra, this has been exploited to investigate the thermodynamic driving forces governing the spectral response. Indeed, the temperature derivative of a spectrum can be used to obtain effective energetic and entropic profiles as a function of the measured frequency. The former can further be used to predict the temperature-dependent spectrum via a van't Hoff relation. However, these approaches are not directly applicable to nonlinear, complex-valued spectra, such as vibrational sum-frequency generation (SFG) or two-dimensional infrared (2D-IR) photon echo spectra. Here, we show how the energetic and entropic driving forces governing such nonlinear spectra can be determined and used within a generalized van't Hoff relation to predict their temperature dependence. The central idea is to allow the underlying energetic profiles to themselves be complex-valued. We illustrate this approach for 2D-IR spectra of water and SFG spectra of the air-water interface and demonstrate the accuracy of the generalized van't Hoff relationship as well as its implications for the origin of temperature-dependent spectral changes.

I. INTRODUCTION

The changes of equilibrium and dynamical properties with temperature offer a key window into the driving forces for chemical processes. While these behaviors represent (literally) textbook examples for chemical equilibria and reaction rates, they have been significantly less well-studied for spectra.

One important example of such a study is that by Hare and Sorensen,¹ who measured the Raman spectrum of dilute HOD in H₂O over a wide range of temperatures. They used these data to carry out a van't Hoff-style analysis of the spectrum at each frequency which yielded an effective enthalpy as a function of the OD vibrational frequency. This approach has subsequently been used by others to probe the temperature dependence of the Raman and infrared (IR) spectra of water and other liquids.^{2–14} Some interpretations of these enthalpy profiles link them directly to the energy required to break a hydrogen-bond in the liquid, which is likely incorrect.¹⁵ Nevertheless, the method is one with significant potential for revealing the factors that shape the spectrum.

In fact, the examination of the temperature dependence of spectra in general, and IR and Raman spectra in particular, has not been used or exploited to its full potential. For example, once the effective enthalpy (or internal energy) profile is obtained, an effective entropy as a function of vibrational frequency is readily accessible, ^{14–16} but, to our knowledge, this has not been obtained in any experimental study. Further, while it is important to recognize that the enthalpies and entropies obtained are effective ones because the spectra include dynamical effects, their fundamental physical relevance is

apparent in the accuracy of a van't Hoff approximation. That is, the effective energy (enthalpy) as a function of frequency can be used to faithfully predict the IR^{15,16} or Raman¹⁴ spectrum over a wide range of temperatures from the spectrum at one temperature. The fact that the spectra, at least for the cases considered so far, are well described by a van't Hoff approximation gives the energy profiles significant practical and interpretative weight.

The advent of nonlinear spectroscopic techniques raises the question of whether the same ideas and van't Hoffian assumptions can be applied to those spectra as well. Addressing these issues is the focus of this Paper. As is illustrated in detail in Sec. II, determining the internal energies (or enthalpies) underlying nonlinear spectra is straightforward in principle. However, invocation of a van't Hoff approximation is more complicated, due to the fact that the spectra are complex-valued and can be zero. Here, we show how this can be readily accomplished simply by allowing the underlying energies and entropies to be complex-valued themselves. Further, we demonstrate that this generalized van't Hoff approximation based on those energies accurately describes the temperature dependence. The different roles of the real and imaginary parts of the energy are elucidated.

We use as examples the vibrational sum-frequency generation (SFG) spectra of the air-water interface and the water two-dimensional infrared (2D-IR) spectra. While the temperature dependence of these nonlinear spectra is significantly less well studied than their linear IR and Raman counterparts, there has been notable work in this direction. In particular, there have been both measurements^{17–19} and simulations^{20–22} of the air-water SFG spectrum at different temperatures. Similarly, experimental studies of the temperature dependence of the 2D-IR spectra of multiple different systems have been reported,^{23–27} along with simulation results primarily focused on water.^{25,28–31} However, none of these studies

a) Electronic mail: wthompson@ku.edu

have explored the energetic and entropic factors underlying the temperature dependence.

This work thus clarifies the thermodynamic driving forces that shape nonlinear spectra and place them on a sound footing by demonstrating their relation to the temperature-dependent behavior. Though the focus here is on vibrational spectra, the approach is general and should also be applicable to electronic and electronic-vibrational spectra. Moreover, while the energy and entropy profiles in this work are generated from direct calculation of the spectrum derivative with respect to temperature, ^{10,15} they can also be obtained from numerical derivatives determined from experimental measurements.

II. THEORY

We can consider the general case of a spectrum given by an intensity $I(\underline{\omega})$ that is everywhere positive; one such example would be the total intensity of a nonlinear spectroscopy measurement, e.g., the homodyne-detected SFG spectrum. Then, one can define an effective free energy given by, $^{14-16}$

$$\Delta A_I(\underline{\omega}) = -k_B T \ln I(\underline{\omega}). \tag{1}$$

The approximation involved is the treatment of the spectral intensity, $I(\underline{\omega})$, as a probability distribution in the frequencies (or one of the frequencies in) $\underline{\omega}$ despite the fact that it generally includes non-trivial dynamical factors (and thus does not possess the qualities of a probability distribution). Indeed, useful insight into non-Condon and dynamical effects can be obtained by comparing $\Delta A_I(\underline{\omega})$ to the rigorous free energy for the underlying frequency distribution, $P(\underline{\omega})$.

A key motivation for invoking the effective free energy is that it can be written in terms of effective internal energy and entropy contributions,

$$\Delta A_I(\underline{\omega}) = \Delta U_I(\underline{\omega}) - T \Delta S_I(\underline{\omega}). \tag{2}$$

It is straightfoward to show that ¹⁵

$$\Delta U_I(\underline{\omega}) = -\frac{1}{I(\underline{\omega})} \frac{\partial I(\underline{\omega})}{\partial \beta} = \frac{I_H(\underline{\omega})}{I(\underline{\omega})}, \quad (3)$$

where $\beta = 1/k_BT$ and the last equality defines $I_H(\underline{\omega})$. The entropy can then be obtained as

$$\Delta S_I(\underline{\omega}) = \frac{1}{T} [\Delta U_I(\underline{\omega}) - \Delta A_I(\underline{\omega})]. \tag{4}$$

These two factors, $\Delta U_I(\underline{\omega})$ and $\Delta S_I(\underline{\omega})$, are measures of the effective thermodynamic driving forces that determine the spectrum and, importantly, its temperature dependence. While we have focused in previous work on the calculation of these properties, ^{14–16} they can be determined experimentally through measurements of $I(\underline{\omega})$ at different temperatures, and this has been done in a

number of cases for both IR and Raman spectra of water and other liquids, as noted in Sec. I.

We note here that the focus of measurements has been on the determination of $\Delta U_I(\underline{\omega})$, despite the importance of entropic factors. Further, interpretations have at times been misguided by treating $I(\underline{\omega})$ as the distribution of instantaneous frequencies (it is not¹⁵) or making assumptions about how $\Delta U_I(\underline{\omega})$ relates to hydrogen-bond making and breaking in water^{1,4} (they largely do not³²). Despite these caveats, this kind of effective thermodynamic analysis can be of great value in understanding the origins of trends and gaining molecular insight. Unfortunately, this approach has been largely overlooked and it should be more widely adopted in spectroscopic studies.

In addition to the mechanistic insight that a thermodynamic analysis can yield, one also obtains the ability to predict behavior over a broad range of temperatures. Namely, the effective internal energy and the spectrum at a given temperature, T_a , can be used in a van't Hoff equation to predict the spectrum at a new temperature T_b ,

$$I(\omega; T_b) = N_I e^{-(\beta_b - \beta_a)\Delta U_I(\underline{\omega})} I(\underline{\omega}; T_a), \tag{5}$$

where $\beta_a=1/k_BT_a$, $\beta_b=1/k_BT_b$, and N_I a normalizing factor that does not affect the line shape and is present because the van't Hoff transformation is not norm-conserving.¹⁵ We have shown that such an approach can quantitatively predict the OH stretch IR spectrum for HOD in D₂O from 280 to 360 K from simulations of the spectrum and its temperature derivative at room temperature.¹⁵

The approach described above cannot be directly applied to phase-resolved nonlinear spectra, like those for SFG or 2D-IR, because the signals are both complex-valued and not positive-definite. In particular, the latter property leads to divergence in the calculation of the internal energy *via* Eq. (3). In the following, we present a simple method for circumventing these issues.

In general, the product of a heterodyne-detected experiment (or a full simulation) is a complex-valued function,

$$\chi(\underline{\omega}) = \chi_r(\underline{\omega}) + i\chi_i(\underline{\omega}) = \chi_m(\underline{\omega})e^{i\phi(\underline{\omega})}, \tag{6}$$

with a total spectral intensity obtained from the square modulus,

$$I(\underline{\omega}) = |\chi(\underline{\omega})|^2 = \chi_r(\underline{\omega})^2 + \chi_i(\underline{\omega})^2 = \chi_m(\underline{\omega})^2.$$
 (7)

Here, $\underline{\omega}$ represents the frequency or frequencies upon which the spectral signal depends. Note that χ_m and ϕ are all real-valued as are $\chi_r(\underline{\omega}) = \chi_m(\underline{\omega})\cos\phi(\underline{\omega})$ and $\chi_i(\underline{\omega}) = \chi_m(\underline{\omega})\sin\phi(\underline{\omega})$. It is possible to choose $\chi_m(\underline{\omega}) > 0$ everywhere (while χ_r and χ_i can be both positive and negative) and we will adopt this choice in the following.

In this notation, the effective thermodynamics underlying the total intensity of a nonlinear spectroscopy measurement, Eq. (7), can be defined based on the magnitude

of the complex spectral signal, $\chi_m(\underline{\omega})$, i.e.,

$$\Delta A_I(\omega) = -k_B T \ln I(\omega) = -2k_B T \ln \chi_m(\omega), \quad (8)$$

with corresponding effective internal energy is then,

$$\Delta U_I(\underline{\omega}) = -\frac{1}{I(\underline{\omega})} \frac{\partial I(\underline{\omega})}{\partial \beta} = -2 \frac{\partial \ln \chi_m(\underline{\omega})}{\partial \beta}, \quad (9)$$

and $\Delta S_I(\underline{\omega})$ is still obtained from this result from Eq. (4).

Of course the total intensity for a nonlinear spectrum such as vibrational SFG or 2D-IR is significantly less interesting (and often harder to interpret) than the underlying phase-resolved components. We now discuss how a complex-valued van't Hoff relationship can be determined for the latter. The answer, in short, is to simply let the effective energies and entropies be themselves complex-valued.

The total intensity free energy $\Delta A_I(\underline{\omega})$ is related to a complex-valued effective free energy associated with the underlying signal,

$$\Delta A_{\chi}(\underline{\omega}) = -k_B T \ln \chi(\underline{\omega})$$

= $-k_B T \ln \chi_m(\omega) - ik_B T \phi(\omega)$. (10)

It is then straightforward to show that

$$\Delta A_I(\underline{\omega}) = \Delta A_{\chi}(\underline{\omega}) + \Delta A_{\chi}^*(\underline{\omega}) = 2\text{Re}[\Delta A_{\chi}(\underline{\omega})] \quad (11)$$

where the * indicates the complex conjugate and Re the real part.

We can define complex-valued internal energy and entropy contributions as

$$\Delta A_{\chi}(\underline{\omega}) = \Delta U_{\chi}(\underline{\omega}) - T \Delta S_{\chi}(\underline{\omega}). \tag{12}$$

The entropy can be obtained from the temperature dependence of the free energy as

$$\Delta S_{\chi}(\underline{\omega}) = -\frac{\partial \Delta A_{\chi}(\underline{\omega})}{\partial T} = \frac{1}{k_B T^2} \frac{\partial \Delta A_{\chi}(\underline{\omega})}{\partial \beta}.$$
 (13)

Inserting Eq. (10) into this expression yields, after some algebra,

$$\Delta S_{\chi}(\underline{\omega}) = \frac{1}{T} \left[-\frac{\partial \ln \chi(\underline{\omega})}{\partial \beta} - \Delta A_{\chi}(\underline{\omega}) \right], \quad (14)$$

for the entropic contribution, which gives

$$\Delta U_{\chi}(\underline{\omega}) = -\frac{\partial \ln \chi(\underline{\omega})}{\partial \beta}$$

$$= -\frac{\partial \ln \chi_{m}(\underline{\omega})}{\partial \beta} - i\frac{\partial \phi(\underline{\omega})}{\partial \beta}$$

$$\equiv \Delta U_{\chi}^{r}(\underline{\omega}) + i\Delta U_{\chi}^{i}(\underline{\omega}) \tag{15}$$

as the internal energy. Note that the real part $\Delta U_{\chi}^{r}(\underline{\omega})$ is equal to $\Delta U_{I}(\underline{\omega})/2$. In the Appendix, we derive expressions for the two derivatives that make up the internal energy. With this internal energy in hand, a van't Hoff approximation can then be applied,

$$\chi(\underline{\omega}; T_b) = N_{\chi} e^{-(\beta_b - \beta_a)\Delta U_{\chi}(\underline{\omega})} \chi(\underline{\omega}; T_a), \qquad (16)$$

where the only difference with the other van't Hoff expressions presented here, Eq. (5), is that χ and ΔU_{χ} are complex-valued. In Sec. IV, we demonstrate that this equation accurately predicts the temperature dependence of simulated SFG and 2D-IR spectra.

It is interesting to explore the implications of these generalized, complex-valued relationships. In terms of the real and imaginary parts of the spectrum, the van't Hoff relationship gives

$$\chi_{r}(\underline{\omega}; T_{b}) = N_{\chi} \left[\chi_{r}(\underline{\omega}; T_{a}) \cos[(\beta_{b} - \beta_{a}) \Delta U_{\chi}^{i}(\underline{\omega})] + \chi_{i}(\underline{\omega}; T_{a}) \sin[(\beta_{b} - \beta_{a}) \Delta U_{\chi}^{i}(\underline{\omega})] \right] \times e^{-(\beta_{b} - \beta_{a}) \Delta U_{\chi}^{r}(\underline{\omega})}$$
(17)

for the real component and

$$\chi_{i}(\underline{\omega}; T_{b}) = N_{\chi} \left[\chi_{i}(\underline{\omega}; T_{a}) \cos[(\beta_{b} - \beta_{a}) \Delta U_{\chi}^{i}(\underline{\omega})] - \chi_{r}(\underline{\omega}; T_{a}) \sin[(\beta_{b} - \beta_{a}) \Delta U_{\chi}^{i}(\underline{\omega})] \right] \times e^{-(\beta_{b} - \beta_{a}) \Delta U_{\chi}^{r}(\underline{\omega})}$$
(18)

for the imaginary component. In these expressions, the real part of the internal energy appears in a typical van't Hoff fashion while the imaginary part acts to rotate the real part of the nonlinear spectrum into the imaginary part and vice versa. Naturally, if the effective internal energy is real, these reduce to the standard van't Hoff expressions for each component of the spectrum. In general, however, they indicate that a component of the real (imaginary) part of the nonlinear spectrum at one temperature becomes part of the imaginary (real) part of the spectrum at other temperatures.

III. COMPUTATIONAL METHODS

A. Calculation of Spectra

The SFG and 2D-IR spectra presented in Sec. IV are calculated using the empirical, or electrostatic, mapping approach that approximates the quantum mechanical vibrational frequencies and transition dipole moments from information directly available in a classical MD simulation.^{33–36} Specifically, each quantity is written in terms of an empirical relationship obtained by correlating the results of explicit quantum mechanical calculations on a cluster to the electric fields computed from classical MD models. We note that there are several other effective approaches for calculating nonlinear vibrational spectra, ^{37–41} which could equally well be used.

For example, the fundamental transition frequency is obtained as $\omega_{01} = c_0 + c_1 \mathcal{E} + c_2 \mathcal{E}^2$, where \mathcal{E} is the (classical MD) electric field component along the OH (OD) bond evaluated at the H (D) atom position and c_0 , c_1 , and c_2 are constants. The constants used in this work for the transition frequency, dipole derivative (μ') , and coordinate matrix element (x_{01}) used to compute the transition dipoles $(\mu_{01} = \mu' x_{01})$ are taken from Auer $et\ al.^{35}$ For

the 2D-IR spectra of HOD in $\rm H_2O$, the empirical maps were taken from Carr $et~al.^{42}$

The resonant part of the SFG spectrum as a function of the IR frequency is obtained as the Fourier transform, 43

$$\chi_{ijk}(\omega_{IR}) = i \int_0^\infty e^{i\omega_{IR}t} \,\varphi_{ijk}(t) \,dt, \qquad (19)$$

where

$$\varphi_{ijk}(t) = \left\langle \alpha_{ij}(0) \,\mu_k(0) \,e^{-i\int_0^t \,\omega_{01}(\tau)d\tau} \right\rangle \,e^{-t/2T_1}, \quad (20)$$

is the dipole-polarizability response function. Here, α and μ are the $0 \to 1$ transition polarizability and dipole moment, respectively. The polarization conditions for the spectrum are labeled by ijk, which determine the tensor and vector elements of α and μ ; here, we consider only the ssp polarization. The n=1 vibrational lifetime is given by T_1 , which is taken to be 700 fs based on experimental measurements; 44 this does not account for the variation in vibrational lifetime for OH groups depending on their hydrogen-bond state at the interface.⁴³ Note that in the calculation of $\varphi_{ijk}(t)$ OH groups with the oxygen atom position below a z-coordinate chosen near the center of the water slab have their contribution multiplied by negative one. In addition, the approach assumes the visible photon is non-resonant and ω_{vis} thus does not enter into the simulated spectrum.

The derivative of the SFG spectrum with respect to temperature or, more precisely, β , can be calculated in the same set of calculations that determine the spectrum itself. We have previously demonstrated this for infrared, ^{15,16} Raman, ¹⁴ and 2D-IR³⁰ spectra by applying fluctuation theory for dynamics. ⁴⁵ Morita and co-workers have pioneered such approaches, ^{10–13} particularly ones aimed at a numerical calculation of the derivative, and applied them to SFG spectra. ¹¹ Briefly, it is straightforward to show that

$$\frac{\partial \chi_{ijk}(\omega_{IR})}{\partial \beta} = -i \int_0^\infty e^{i\omega_{IR}t} \, \varphi_{H,ijk}(t) \, dt, \qquad (21)$$

where

$$\varphi_{H,ijk}(t) = \left\langle \delta H(0) \, \alpha_{ij}(0) \, \mu_k(0) \, e^{-i \int_0^t \, \omega_{01}(\tau) d\tau} \right\rangle \, e^{-t/2T_1}. \tag{22}$$

Here, $\delta H(0) = H(0) - \langle H \rangle$ is the fluctuation of the total energy from its average value at t = 0, with H the total system Hamiltonian. We have neglected the temperature dependence of the vibrational lifetime T_1 , which is known from experimental measurements^{25,46} to be weak; for cases where this contribution is important, it can be straightforwardly included.

The approach for calculating the 2D-IR spectra are analogous, but more complicated as multiple time correlation functions, each of which depends on three time intervals, must be calculated. The details of the approach used, including the calculation of the β derivatives, can be found in our recent publication.³⁰ The underlying framework for the calculations of the spectra themselves is that introduced by Skinner and co-workers.^{47,48}

B. Molecular Dynamics

All MD simulations were performed using the Large-Scale Atomic/Molecular Massively Parallel Simulator (LAMMPS). 49,50 Each simulation consisted of 343 SPC/E water molecules 51 in a rectangular simulation cell of xy-dimensions of 21.725311 Å \times 21.725311 Å and z-dimension of 80 Å. The Lennard-Jones and Coulombic interactions were cut off at 10.5 Å, and the long-range electrostatics were included by a particle-particle particle mesh Ewald description with a tolerance of 10^{-4} . A time step of 1 fs was used in all cases.

The response function in Eq. (20) was calculated using the trajectory sampling approach introduced previously. Namely, a constant number, volume, and temperature (NVT) trajectory (with the temperature controlled by a Nosé-Hoover thermostat 53,54 with time constant 100 fs) is propagated for 2 ns and restart files are written every 1 ps. Each of the 2000 restart files is then used to initiate a short, 10 ps, NVE trajectory from which the SFG response function and its temperature derivative are calculated. In calculating the derivatives, 20 such NVT trajectories at 298.15 K are used; for reference spectra at other temperatures, one 1 ns NVT trajectory is used (corresponding to 1000 NVE trajectories).

Errors in the computed results were obtained by block averaging using 20 blocks (each block representing 2000 NVE trajectories) and are reported as 95% confidence intervals using the Student's t-distribution.⁵⁵

The simulations to compute the 2D-IR spectra were similar, but of 343 SPC/E water molecules in a cubic simulation cell of side length 21.725311 Å. For this system, four 2 ns NVT trajectories were propagated with restart files written every 1 ps. The latter were used to initiate 20 ps NVE trajectories for calculation of the response function and its derivatives at 298.15 K. All other simulation parameters are the same as described above. The direct calculations at other temperatures were obtained from 1000 NVE trajectories of length 10 ps each, pulled from a 1 ns NVT trajectory.

IV. RESULTS

In this Section, we apply the generalized van't Hoff description to the vibrational SFG spectrum of the airwater interface and the 2D-IR spectrum of water. In both cases we make use of isotopic dilution to remove effects of resonant vibrational coupling. These serve as useful and general examples. We use the fluctuation theory for dynamics⁴⁵ approach to determine the derivative of the spectra with respect to temperature as described in Sec. III A, though experimentally (or computationally) this can be done through measuring (calculating) the spectra at multiple temperatures.

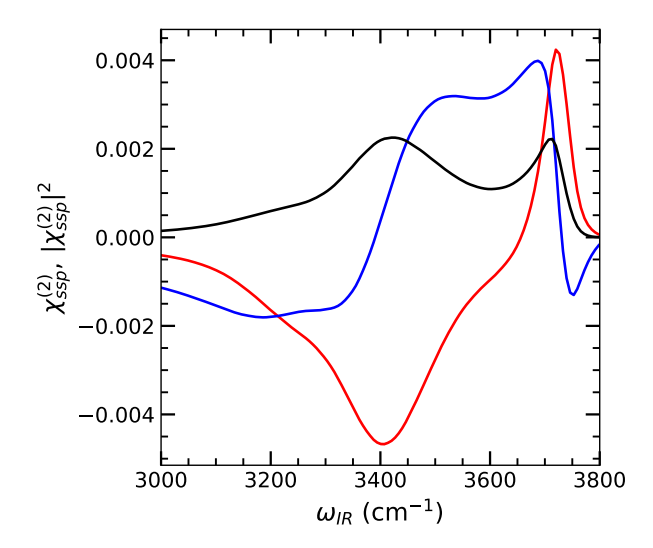


FIG. 1: The real (blue) and imaginary (red) components of the phase-resolved vibrational SFG spectrum of the air-water interface are shown along with the total intensity (black), Eq. (7). Shaded regions (smaller than the linewidth here) indicate 95% confidence intervals.

A. Sum-Frequency Generation Spectra

1. Water-Air SFG Spectra

We first calculated the vibrational SFG spectrum for the air-water interface system, described in Sec. III B, using the empirical mapping approach detailed in Sec. III A. The real and imaginary parts of the spectrum for the ssp polarization conditions are shown, together with the total intensity, in Fig. 1. The results represent the spectrum of dilute HOD in D_2O as resonant vibrational coupling is neglected in the description. The spectra are in good agreement with those obtained by Auer and Skinner, ⁴³ which in turn are in accord with measurements by Raymond $et\ al.^{56}$

The imaginary part of the spectrum is the component that carries the key information about the molecular system. The sign of $\operatorname{Im}[\chi^{(2)}_{ssp}]$ reflects the direction of the OH groups at that vibrational frequency. Thus, the positive peak around 3720 cm⁻¹ reflects OH groups at the interface that are dangling into the air side of the interface.³⁷ The remainder of $\text{Im}[\chi^{(2)}_{ssp}]$ below $\sim 3665 \text{ cm}^{-1}$ is negative, indicative of OH groups that are hydrogen bonded to other water molecules and thus pointing into the water. This negative-going signal is largest in magnitude around 3400 cm⁻¹, significantly redshifted from the dangling OH moieties. The real part of the SFG spectrum is less intuitive to interpret. It has a small negative peak around 3750 cm⁻¹, a large, bimodal peak between 3395 and 3730 cm^{-1} , and a small amplitude, broad feature at lower frequencies.

The total SFG intensity given by Eq. (7) is also shown

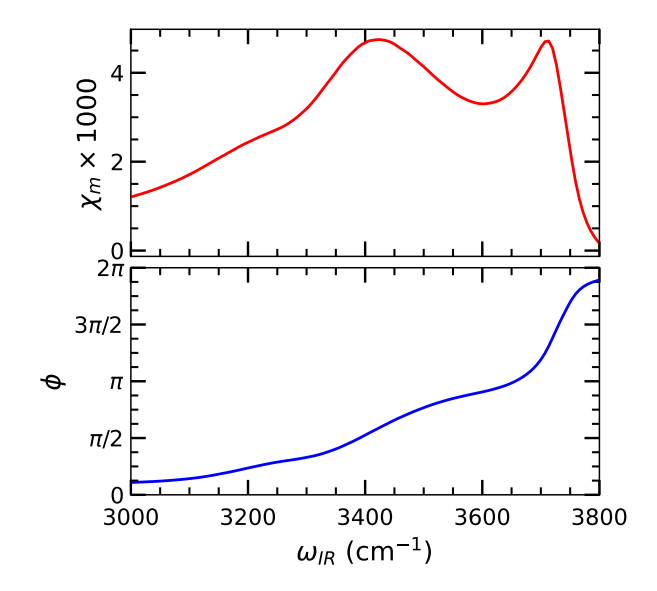


FIG. 2: The amplitude, χ_m (top panel, red line), and the phase, ϕ (bottom panel, blue line), of the complex SFG spectrum shown in Fig. 1 are shown as a function of the vibrational frequency; see Eq. (6).

for comparison in Fig. 1. It has two peaks of roughly equal intensity. The first is narrower and peaks at $3712~{\rm cm}^{-1}$. The second is broad and peaks around $3420~{\rm cm}^{-1}$. Of note here are the differences with ${\rm Im}[\chi^{(2)}_{ssp}]$ in terms of the shifts in frequency of the dangling and hydrogen-bonded peaks as well as the lack of information about the directionality of the OH bonds contributing at different frequencies. This well-known behavior is a key motivator for understanding the temperature dependence of the complex SFG signal rather than only the total intensity.

The real and imaginary components of the SFG spectrum can be converted into an amplitude, $\chi_m(\omega)$, and phase, $\phi(\omega)$ as noted in Eq. (6). These are plotted in Fig. 2 as a function of the vibrational frequency, ω_{IR} . As noted above, the amplitude χ_m is simply the square root of the total (non-phase-resolved) SFG intensity which is shown in Fig. 1. The phase (which we have chosen such that it is continuous between $-\pi$ and π) then determines the sign of the real and imaginary parts of the spectrum. That is, as ϕ passes $3\pi/2$ and $\pi/2$ the real part of the spectrum changes sign and as it passes π the imaginary part changes sign.

2. Water-Air SFG Spectra Derivatives and Energies

As was shown in Sec. II, the energetic driving forces that underlie the complex SFG spectra can be determined from the temperature (or, more precisely, β) derivatives of the amplitude and phase shown in Fig. 2. Equations for these are given in the Appendix in terms of the β derivatives of the real and imaginary compo-

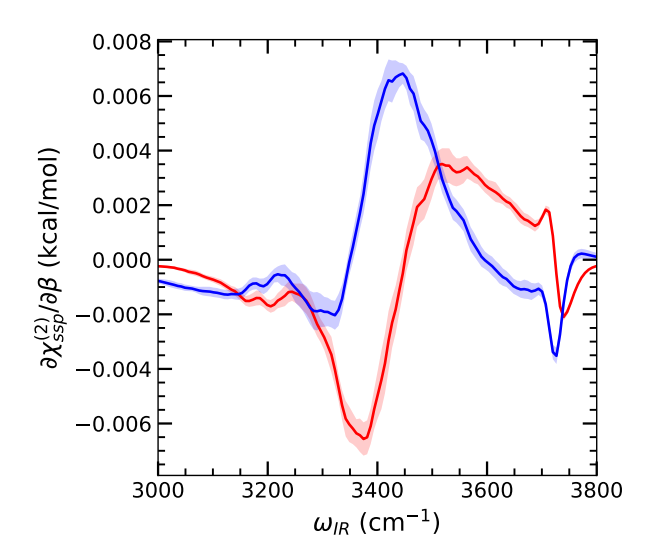


FIG. 3: Derivatives with respect to β of the real (blue) and imaginary (red) components of the phase-resolved vibrational SFG spectrum of the air-water interface at 298.15 K are shown. Shaded regions indicate 95% confidence intervals.

nents of the spectrum. The latter can be calculated using the fluctuation theory for dynamics approach, which we have previously applied to the calculation of the temperature derivatives of infrared, ^{15,16} Raman, ¹⁴ and two-dimensional infrared photon echo spectra. ³⁰

The β derivatives of the real and imaginary components of the air-water SFG spectrum at room temperature were calculated according to the fluctuation theory for dynamics approach outlined in Sec. III A. The results are shown in Fig. 3. First consider the imaginary component derivative, $\partial \text{Im}[\chi_{ssp}^{(2)}]/\partial \beta$. It can be roughly viewed as composed of two sigmoidal peaks, one centered around the dangling OH peak in the SFG spectrum and the other around the hydrogen-bonded OH peak. We see the derivative changes from positive to negative around 3724 cm⁻¹, a frequency just higher than the maximum of the dangling OH peak. The magnitude of the derivative is larger for the frequencies in the hydrogen-bonded region. It reaches a minimum around 3375 cm^{-1} and changes sign from negative to positive at $\sim 3450 \text{ cm}^{-1}$. Note that, because the SFG spectrum in this frequency range is negative, the interpretation of the sign of the derivative is also flipped from that in the positive-going dangling OH region.

The derivative of the real component of the spectrum, $\partial \text{Re}[\chi^{(2)}_{ssp}]/\partial \beta$, has a large, asymmetric positive peak between 3350 and 3575 cm⁻¹, which peaks around 3440 cm⁻¹, this is shifted to lower frequencies compared to the positive peak in the real part of the SFG spectrum itself. At frequencies lower than this the derivative is small and negative. At higher frequencies the derivative has a negative peak centered around 3724 cm⁻¹, *i.e.*, around the frequency of the dangling OH peak in

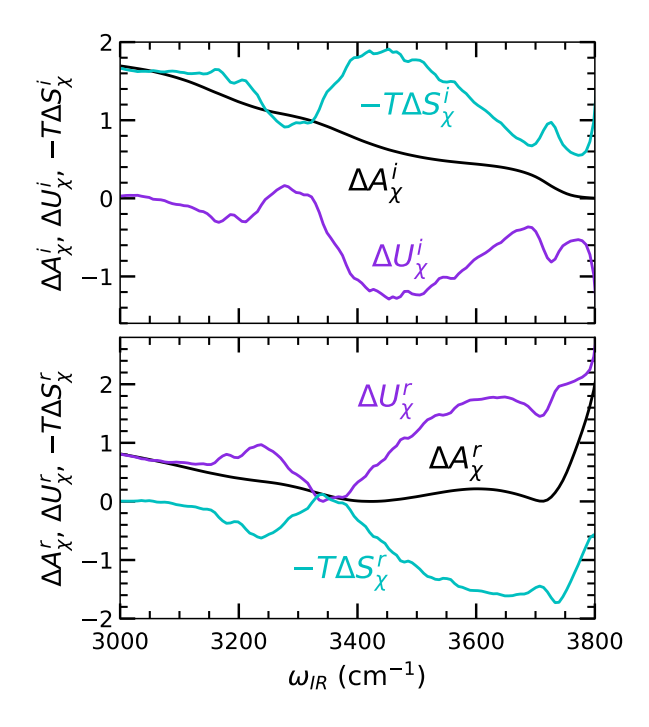


FIG. 4: The imaginary (top panel) and real (bottom panel) part of the free energy ΔA (black lines), internal energy ΔU (purple lines), and entropy contribution $-T\Delta S$ (cyan lines) are shown (in kcal/mol) for the air-water SFG spectrum as a function of the vibrational frequency.

 $\operatorname{Im}[\chi_{ssp}^{(2)}].$

Interpreting these derivatives is most straightforwardly done by converting them to (complex-valued) internal energy and entropy contributions as described in Sec. II. This gives insight into the thermodynamic driving forces that determine the temperature dependence of the spectra and hence the spectral features themselves. The real and imaginary free energies, defined in Eq. (10), are shown in Fig. 4. These simply reflect the negative logarithms of the amplitude and phase shown in Fig. 2, so that ΔA_{χ}^{i} is monotonically decreasing with ω_{IR} and ΔA_{χ}^{r} has minima at $\omega_{IR} = 3400$ and 3720 cm⁻¹ (the locations of the peak maxima of the total SFG intensity shown in Fig. 1).

The complex-valued internal energy and entropy contributions to the free energy are also shown in Fig. 4. We first consider the real component of the internal energy which determines the more traditional van't Hoff behavior of the spectrum, as shown in Eqs. (17) and (18). There is a broad global minimum in ΔU_χ^r between ~ 3340 and $3380~{\rm cm}^{-1}$, indicative of the most energetically favored OH frequencies in the SFG signal. This falls in the range of the broad negative peak of the imaginary SFG spectrum that corresponds to hydrogenbonded OHs pointing into the water. At lower frequencies, ΔU_χ^r reaches a local maximum at 3240 cm⁻¹ after which it becomes relatively flat. Toward higher frequen-

cies, the internal energy rises slowly and nearly monotonically; it has a prominent local minimum at 3710 cm $^{-1}$ in the dangling OH region, though the internal energy is $\sim 1.4~\rm kcal/mol$ higher there than at the global minimum.

The real component of the entropic contribution, $-T\Delta S_{\chi}^{r}$ illustrates a strong energy-entropy compensation effect. Namely, $-T\Delta S_{\chi}^{r}$, is nearly a mirror image of ΔU_{χ}^{r} . It has a broad global maximum between ~ 3340 and 3380 cm^{-1} that reflects significant ordering for these energetically favorable hydrogen-bonding arrangements. The entropy contribution then falls off to both higher and lower frequencies in a way that largely cancels the internal energy. It is the incomplete cancellation of the two contributions that determines the free energy. One particularly notable feature of the entropy profile is that it has a distinct minimum in the dangling OH region around 3735 cm⁻¹, suggestive of the more disordered state of these non-hydrogen-bonded groups, that is not mirrored in ΔU_{γ}^r . The different behaviors of ΔU_{γ}^r and $-T\Delta S_{\gamma}^r$ in this high frequency region lead to the dangling OH peak (minimum) in the SFG spectrum (free energy).

The consequences of the imaginary components of the internal energy and entropy contributions, shown in the top panel of Fig. 4 are more challenging to interpret. What is clear from Eqs. (17) and (18) is that ΔU_{ν}^{i} acts, as the temperature is changed, to rotate the real part of the SFG spectrum into the imaginary part and vice versa. Thus, the larger ΔU_{χ}^{i} , the bigger this effect; if $\Delta U_{\chi}^{i} = 0$, the behavior with temperature is determined by traditional van't Hoff relations for the real and imaginary components of the spectrum separately. We can see from Fig. 4 that ΔU_{χ}^{i} has a broad minimum between ~ 3420 and $3520~{\rm cm}^{-1}$. Moving to lower frequencies, ΔU_{χ}^{i} rises through a wide maximum after which it decreases before rising to zero. On the higher frequency side of the minimum, the internal energy rises steadily through a local maximum around 3690 cm⁻¹, which is followed by a sharp local minimum at $3725~\mathrm{cm}^{-1}$ (corresponding to the dangling OH peak). This behavior of the internal energy is nearly perfectly mirrored by the entropic contribution, $-T\Delta S_{\chi}^{i}$, except that ΔU_{χ}^{i} decreases more rapidly with increasing ω_{IR} across the entire range of frequencies, giving rise to the monotonically decaying imaginary component of the free energy, ΔA_{ν}^{i} .

3. Generalized van't Hoff Predictions

In addition to providing insight into the thermodynamic driving forces determining the spectrum, the internal energy contributions can be used to predict the nonlinear spectrum as a function of temperature. Here, we illustrate this for the air-water SFG spectrum using the internal energies determined from the temperature derivatives of the spectrum at room temperature and presented in the previous section. Specifically, we have applied Eqs. (17) and (18) using the complex-valued SFG spectrum and the complex-valued internal energies at 298.15 K shown in Figs. 1 and 4, respectively, to predict the spectrum at temperatures from 280 to 360 K. Each spectrum is normalized so that the maximum is equal to one.

The results are shown in Fig. 5 where they are compared to direct calculations of the SFG spectrum at each temperature. The agreement of the predicted spectra based on the generalized van't Hoff relation and the directly calculated ones are very good. The imaginary component of the spectrum shows a modest 10 cm⁻¹ blueshift of the dangling OH peak with increasing temperature. The broad, negative-going peak corresponding to hydrogen-bonded OHs is also blueshifted with temperature from ~ 3385 to $3450~\rm cm^{-1}$ between 280 and 360 K and it simultaneously broadens. The van't Hoff predictions differ only slightly from the direct calculations due to statistical noise in the internal energy, e.g., note the oscillations in the predicted spectrum around the directly calculated result at 360 K.

The real component of the spectrum likewise is well-predicted by the generalized van't Hoff relation, except for some error due to noise in the internal energy. The negative peak in the dangling OH region exhibits only a 3 cm⁻¹ blueshift in this temperature range. However, the large, bimodal peak at intermediate frequencies becomes more asymmetric with increasing temperature; the peak on the blue side increases in prominence, but does not shift, while the low-frequency peak blueshifts by $\sim 30~{\rm cm}^{-1}$ and decreases in relative magnitude.

We can understand these trends in the temperature dependence by isolating the effects of the real and imaginary parts of the internal energy. This is shown in Fig. 6 where the SFG spectra are predicted as a function of temperature assuming $\Delta U_{\chi}^{i}=0$. In other words, these predictions assume that the imaginary part of the spectrum is determined only by the imaginary spectrum at 298.15 K and a van't Hoff exponential scaling based on ΔU_{χ}^{r} and similarly for the real part of the spectrum. In the context of Eqs. (17) and (18), this means there is no rotation of the real part of the spectrum into the imaginary part (and vice versa) as the temperature is changed.

The shortcomings of this approximation are clear from Fig. 6 where the simplified predictions depart notably from the directly calculated spectra. In particular, in the imaginary part of the spectrum, while the dangling OH peak is still well described, the blueshift of the negative-going hydrogen-bonded peak is significantly underestimated and its amplitude decreases too rapidly. This leads to discrepancies in the 3400-3700 cm⁻¹ range. Similarly, in the real part of the spectrum, this approximate description underestimates the blueshift of the peak around 3500 cm⁻¹ and its decrease in amplitude with increasing temperature. In addition, the decreasing amplitude with temperature of the peak in the dangling OH region is underestimated.

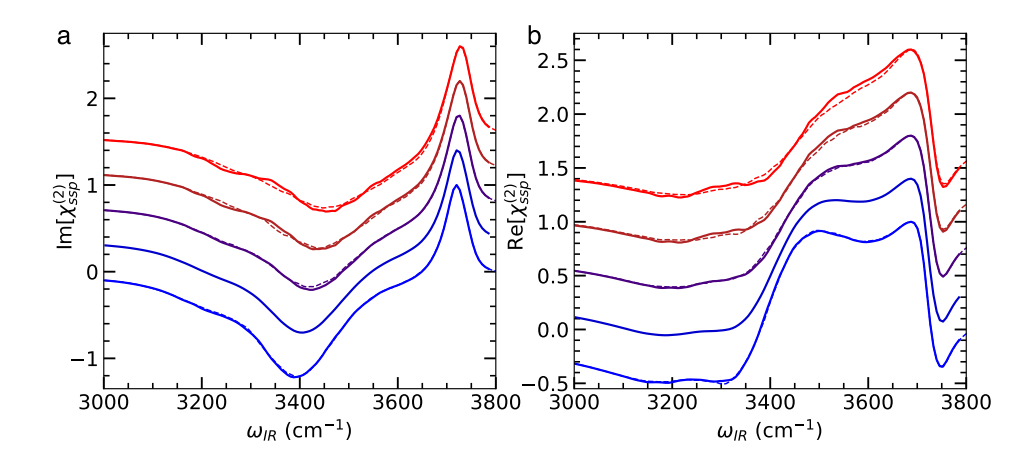


FIG. 5: The predicted a) imaginary and b) real components of the air-water SFG spectrum, $\chi_{ssp}^{(2)}(\omega_{IR})$, (solid lines) are compared to directly calculated results at each temperature (dashed lines of the same color); each spectrum is normalized to a maximum value of one. Results are shown for 280, 298, 320, 340, and 360 K (bottom to top; blue to red); above 280 K each curve is shifted by 0.4 for clarity.

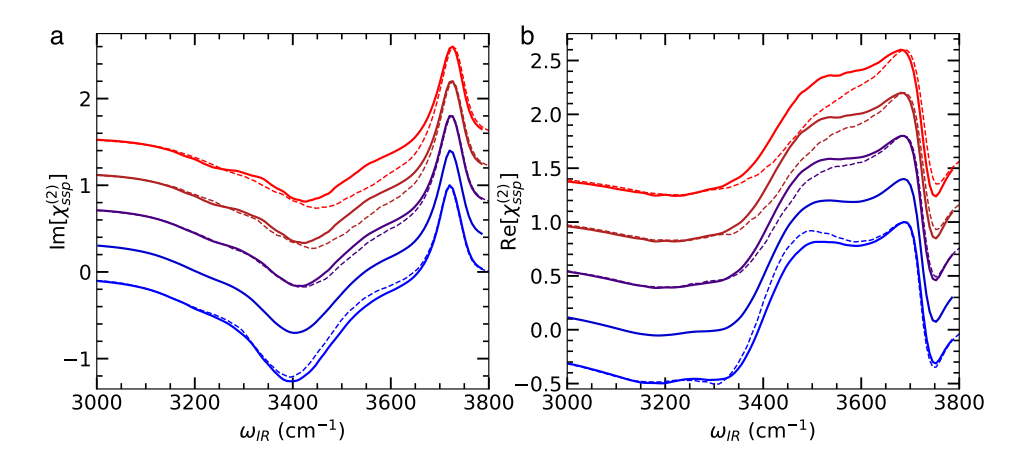


FIG. 6: Same as Fig. 5 except that the predicted spectra are obtained by assuming $\Delta U_i(\omega_{IR}) = 0$.

B. Two-Dimensional Infrared Spectra

1. HOD/H₂O 2D-IR Spectra

We also considered the case of the 2D-IR spectra of dilute HOD in H_2O , probing the dynamics of the OD stretch. The results of the empirical mapping-based simulations of the spectra at 298.15 K are shown in Fig. 7 for two different waiting times, $T_w = 0$ and 1 ps. The real part of the spectrum, labeled as $\text{Re}[\chi]$, shows the expected change with waiting time. Namely, the peaks show significant correlation between the initial frequency, ω_1 , and the final frequency, ω_3 , as they are elongated at $T_w = 0$ ps in a direction parallel to the diagonal, but are significantly more rounded and elongated parallel to the ω_1 axis at the 1 ps waiting time. This is consistent with the relatively rapid spectral diffusion time of $\sim 1-1.5 \text{ ps.}^{57}$

In the context of the approach described in Sec. II,

we also plot the imaginary component of the spectrum, $\text{Im}[\chi]$ in Fig. 7, which exhibits a different structure than the real contribution, but also shows the loss of correlation between the initial and final frequency at the longer waiting time.

The real and imaginary parts of the 2D-IR spectrum can be converted to a magnitude χ_m and phase ϕ , as given in Eq. (6), and these are also plotted in Fig. 7. The magnitude $\chi_m(\omega_1,\omega_3)$ is positive everywhere and centered around the peak for the OD stretch in the IR spectrum. 30,42 It also displays the loss of correlation with waiting time between the initial and final frequencies through a change in the elongation of the central peak. The sign of the real and imaginary spectra are determined by the phase $\phi(\omega_1,\omega_3)$, which reaches $\pi/2$ at the nodal line of Re[χ] that separates the $0 \to 1$ and $1 \to 2$ peaks. Thus, while the general feature that ϕ increases monotonically with ω_3 is observed at both waiting times, the slope of the contours approaches zero as T_w grows.

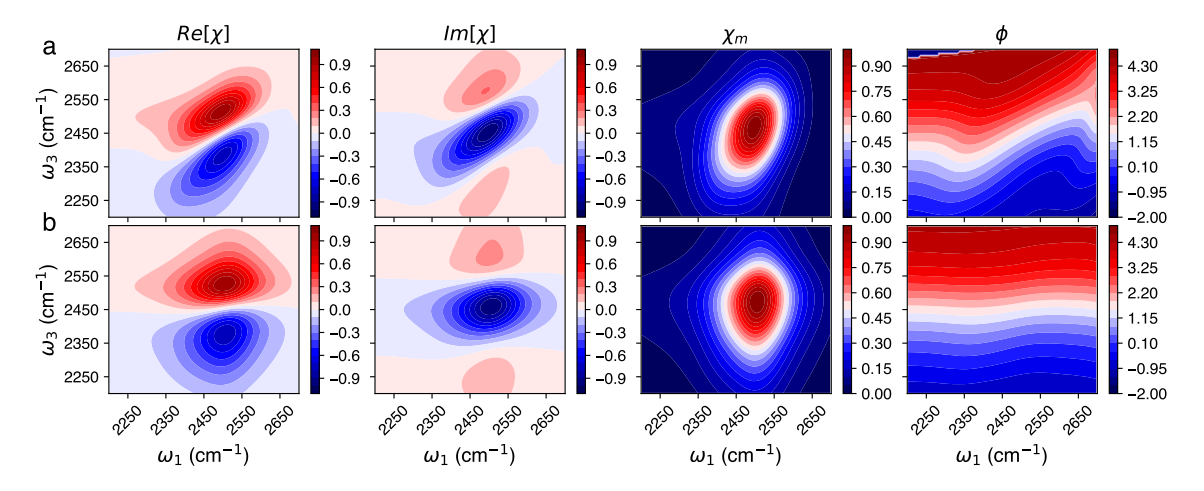


FIG. 7: Calculated 2D-IR spectra for HOD/H₂O at 298.15 K are plotted; from left to right are shown the real component, Re[χ], the imaginary component, Im[χ], and the magnitude, χ_m , and phase, ϕ , of the complex signal. Results are shown for waiting times of a) $T_w = 0$ ps, and b) $T_w = 1$ ps.

2. HOD/H₂O 2D-IR Spectra Derivatives and Energies

As with the SFG spectra, the derivatives of the 2D-IR spectra can be obtained from a time correlation function that includes both the normal spectral response function correlated with the fluctuation of the total system energy. We have previously demonstrated this for 2D-IR spectra of $\mathrm{HOD/H_2O}$ with and without urea. ³⁰ Here, we use the calculated derivatives with Eq. (15) to determine the real and imaginary components of the effective internal energy of the spectra. These are shown in Fig. 8 for $T_w = 0$ and 1 ps. (Note that, as in the case of IR spectra, these effective energies can exhibit effects due to subtle line shape changes and greater statistical noise that appear outside the main peaks of the spectra.)

The interpretation of these effective internal energy surfaces is not as straightforward as the one-dimensional profiles for IR, ¹⁵ Raman, ¹⁴ or SFG spectra (Fig. 4). Certainly, greater insight will be developed by examination of such surfaces for a variety of different systems. At this point, however, one perspective is to view them in the context of the generalized van't Hoff relation (discussed in greater detail below). Then, $\Delta U_r(\omega_1, \omega_3)$ reflects the favorability of initial and final frequency pairs as a function of temperature: Lower ΔU_r values indicate regions of the spectrum that will increase in intensity as temperature is lowered while larger magnitudes of ΔU_i are associated with greater rotation of the real and imaginary components of the spectra with temperature changes.

Within this viewpoint, we see that the ΔU_r surfaces plotted in Fig. 8 do not share the same shape as the 2D-IR spectra or the magnitude χ_m . Rather, they show a broad minimum valley that encompasses both the $0 \to 1$ and $1 \to 2$ peaks in Re[χ] and extends down to lower values of ω_3 (the final, or probed, frequency). This minimum value becomes more parallel to the ω_3 axis at the longer waiting time. The ΔU_r rises outside of this region,

but most strongly as the initial frequency, ω_1 is increased.

The imaginary component of the internal energy shows a different structure. It also does not follow the shape of the spectra themselves, and changes sign moving across $\text{Re}[\chi]$ peaks. It tends to be negative in the region of the $0 \to 1$ peak of the real spectrum with the positive ΔU_i values overlapping primarily with the $1 \to 2$ peak. Generally, ΔU_i is small in magnitude, but as will be shown below, significant.

The corresponding entropic contributions are also shown in Fig. 8. These, combined with the internal energies give the effective complex free energy, which is equivalent to the 2D-IR spectra through inversion of Eq. (10). In the generalized van't Hoff interpretation, the effective entropies correspond to the temperature-independent part of the spectrum as can be seen by their absence in Eq. (16). The real component of the entropy, $-T\Delta S_r$, tends to be most favorable at higher ω_1 and ω_3 , corresponding to weaker, but more loosely constrained, hydrogen bonds. The imaginary component generally decreases with increasing ω_3 and is lowest for higher values of this final frequency.

3. Generalized van't Hoff Predictions

We have used the effective internal energies for the 2D-IR spectra, given in Fig. 8, to predict the temperature dependent spectra (real components) from 280-360 K. The inputs are the spectra at 298.15 K and the effective internal energies; we normalize the resulting predicted 2D-IR spectra to be one at the maximum value. These generalized van't Hoff-predicted spectra are shown in Fig. 9 where they are compared to spectra directly calculated from simulations at each temperature.

The predicted spectra are in excellent agreement with the direct calculations across the full range of tempera-

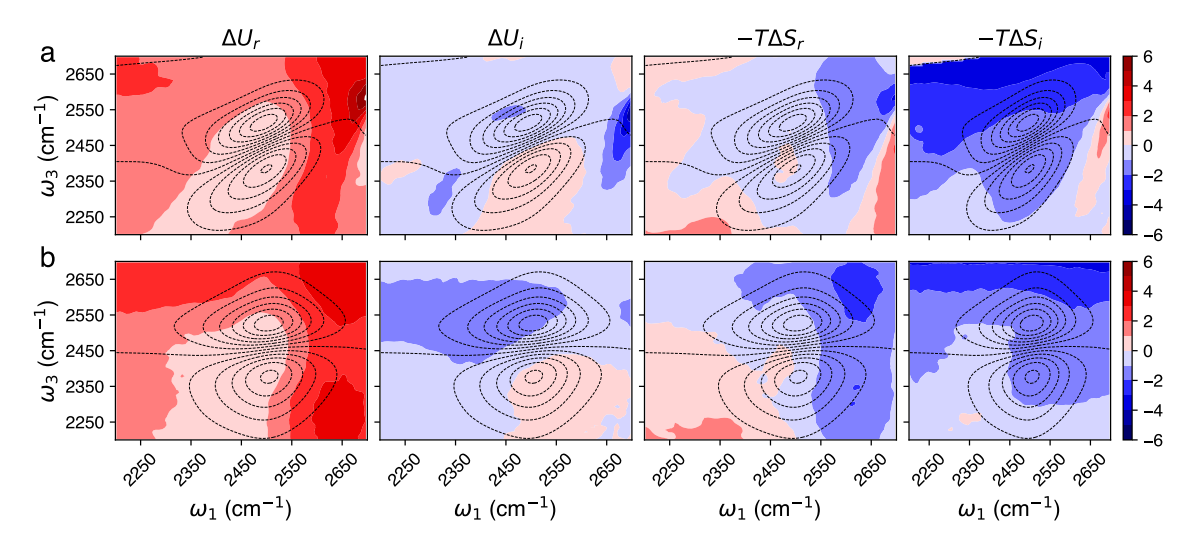


FIG. 8: Calculated energetic contributions to the 2D-IR spectra for HOD/H₂O at 298.15 K are plotted (in kcal/mol); from left to right are shown the real, ΔU_r , and imaginary, ΔU_i , internal energies and the real, $-T\Delta S_r$, and imaginary, $-T\Delta S_i$, entropic contributions to the free energy. Results are shown for waiting times of a) $T_w = 0$ ps, and b) $T_w = 1$ ps. The real components of the 2D-IR spectra are also shown (dashed black contour lines) for reference.

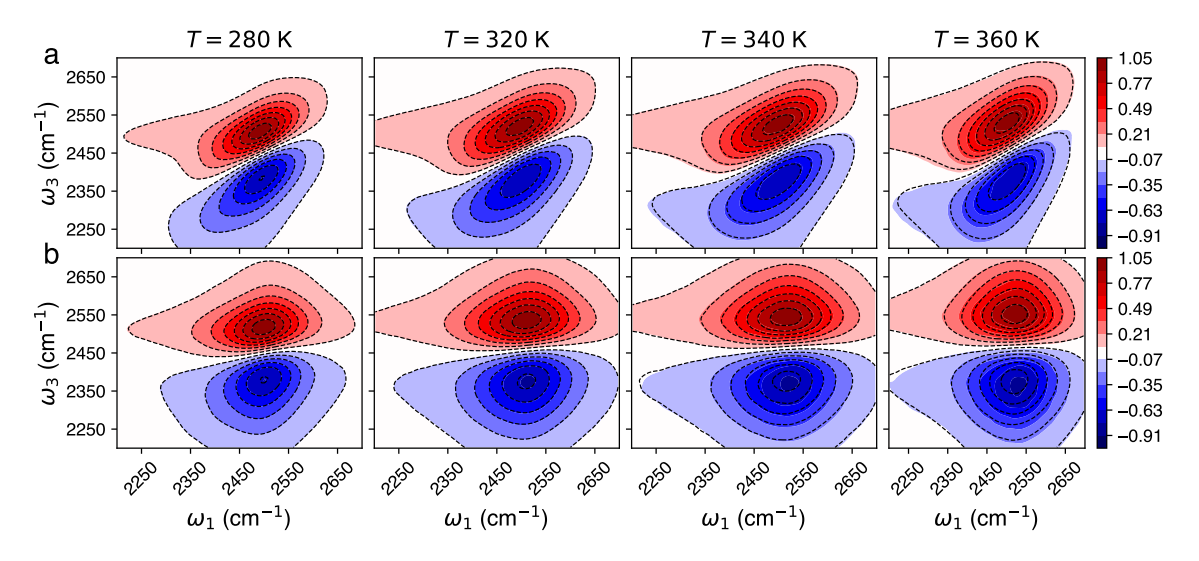


FIG. 9: Predicted real component of the 2D-IR spectra for HOD/H_2O using the generalized van't Hoff approach (colored contours) are compared to directly calculated spectra (dashed black contour lines) at 280, 320, 340, and 360 K. Results are shown for waiting times of a) $T_w = 0$ ps, and b) $T_w = 1$ ps.

tures. At 280 and 320 K the generalized van't Hoff spectra are in essentially perfect agreement with the directly calculated results. At 340 and 360 K we see some small differences between the two, primarily in the negative-going $1 \rightarrow 2$ peak. This is likely due to incomplete convergence in the effective internal energy (which is magnified by its presence in the exponential of the van't Hoff expression, Eq. (16).

It is also useful to compare these results to our recent efforts on the temperature dependence of 2D-IR spectra.³⁰ We observed that a Taylor series expansion in

the inverse temperature, β , is adequate at nearby temperatures (within ~ 20 K), but is a poor description outside this range. This Taylor series approach represents the first-order approximation to the generalized van't Hoff relation presented in this work.

It is useful to probe the "generalized" aspect of the present van't Hoff relation given by Eq. (16). We do this in the same way as for the SFG spectra, by assuming that $\Delta U_i = 0$ such that the generalized van't Hoff prediction reduces to a traditional van't Hoff relationship with no rotation of the real and imaginary components

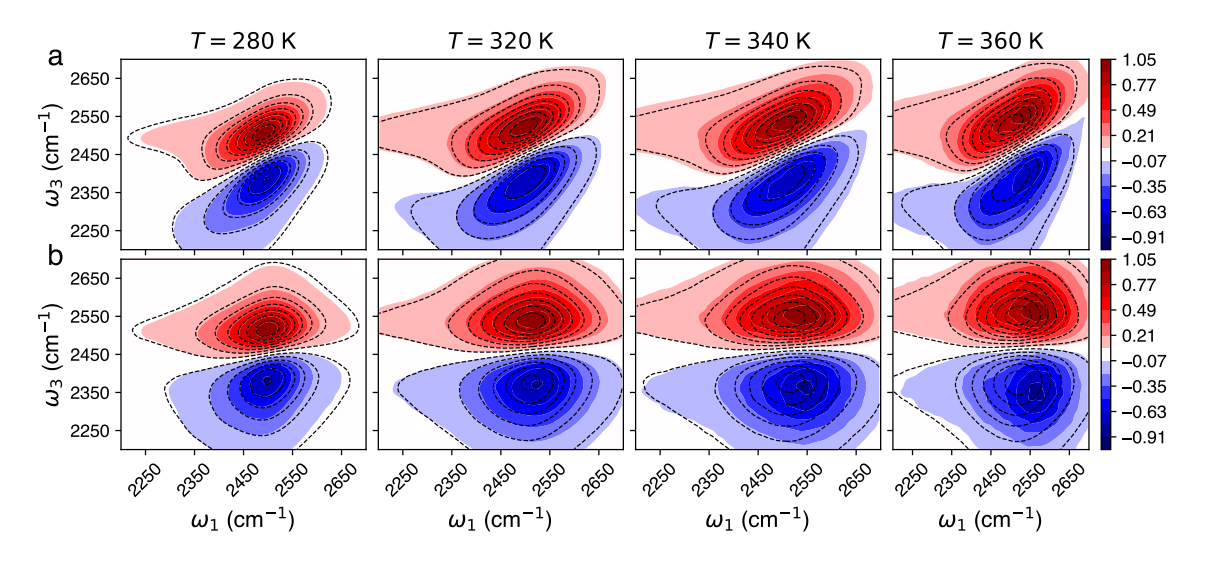


FIG. 10: Same as Fig. 9 except the predicted spectra assume $\Delta U_i(\omega_1, \omega_3) = 0$.

of the spectra. These results are shown in Fig. 10 for temperatures of 280-360 K. We can see that this normal van't Hoff relation predicts the spectra reasonably well for 280 and 320 K, but does increasingly poorer at higher temperatures. In particular, it predicts that the peak positions for both the $0 \to 1$ and $1 \to 2$ peaks shift further to the blue for the initial frequency ω_1 . It similarly overpredicts the blueshift for the $0 \to 1$ peak in ω_3 while exhibiting too large a redshift in the $1 \to 2$ peak in the final frequency.

V. CONCLUSIONS

We have shown how the van't Hoff relationship can be generalized to predict the temperature dependence of nonlinear, complex-valued spectra. The central features of this approach are an effective free energy as a function of frequency that is determined directly from the spectra and corresponding internal energy and entropic contributions that can be obtained from the temperature dependence of the spectra. These provide both key insight into the effective thermodynamic driving forces that determine a spectrum as well as the ability to predict the spectrum over a wide range of temperatures. The changes with temperature arise from two factors. The real component of the internal energy acts in a traditional van't Hoff exponential scaling with inverse temperature while the imaginary component serves to rotate the real component of the spectrum into the imaginary component with temperature and vice versa.

We illustrate the approach on the vibrational sumfrequency generation spectrum of the air-water interface. We show that the generalized van't Hoff relationship accurately predicts SFG and 2D-IR spectra at temperatures from 280 to 360 K based only on the spectra and their temperature derivatives at room temperature. The derivative is, in this work, obtained from a fluctuation theory for dynamics approach; this approach is general and we have, for example, recently applied it to calculation of the temperature derivatives of 2D-IR spectra.³⁰ However, the derivatives can also be obtained numerically from measured or calculated spectra at nearby temperatures. Thus, this approach can be applied to the results of experimental measurements. In this context, the complex-valued internal energies and corresponding entropies obtained from such an analysis – though they are effective ones because the spectra necessarily include dynamical factors – can be viewed as the fundamental measures of the thermodynamic driving forces that determine the spectral features. While we have used SFG and 2D-IR spectra as an illustration, the approach is general and can be straightforwardly applied to other nonlinear spectra, including those probing vibrational, electronic, or vibrational and electronic motions.

These results add to other recent evidence providing strong impetus for greater focus on the temperature dependence of spectra. Such studies, both experimental and computational, can improve our fundamental understanding of the factors determining the spectra.

ACKNOWLEDGMENTS

The authors thank Profs. Carlos R. Baiz, Sean Garrett-Roe, and Brian B. Laird for useful discussions and comments. This work was supported by the National Science Foundation under Grant CHE-2102656. The calculations were performed at the University of Kansas Center for Research Computing (CRC), including the BigJay cluster resource funded through NSF Grant MRI-2117449.

AUTHOR DECLARATIONS

Conflict of Interest

The authors have no conflicts to disclose.

Author Contributions

Ashley K. Borkowski: Software (equal); writing – original draft (supporting); writing – review and editing (equal). Hasini S. Senanayake: Software (equal); writing – original draft (supporting); writing – review and editing (equal). Ward H. Thompson: Conceptualization (lead); funding acquisition (lead); software (equal); writing – original draft (lead); writing – review and editing (equal).

DATA AVAILABILITY

The data that support the findings of this study are available from the corresponding author upon reasonable request.

APPENDIX

Here we relate the β derivatives of χ_r and χ_i to those of χ_m and ϕ . We first note that

$$\frac{\partial \chi_r(\underline{\omega})}{\partial \beta} = \frac{\partial}{\partial \beta} \left[\chi_m(\underline{\omega}) \cos \phi(\underline{\omega}) \right]
= \frac{\partial \chi_m(\underline{\omega})}{\partial \beta} \cos \phi(\underline{\omega}) - \chi_m(\underline{\omega}) \sin \phi(\underline{\omega}) \frac{\partial \phi(\underline{\omega})}{\partial \beta}
= \frac{1}{\chi_m(\underline{\omega})} \frac{\partial \chi_m(\underline{\omega})}{\partial \beta} \chi_r(\underline{\omega}) - \chi_i(\underline{\omega}) \frac{\partial \phi(\underline{\omega})}{\partial \beta}. \quad (A1)$$

Similarly, we have

$$\frac{\partial \chi_i(\underline{\omega})}{\partial \beta} = \frac{\partial}{\partial \beta} \left[\chi_m(\underline{\omega}) \sin \phi(\underline{\omega}) \right]
= \frac{1}{\chi_m(\underline{\omega})} \frac{\partial \chi_m(\underline{\omega})}{\partial \beta} \chi_i(\underline{\omega}) + \chi_r(\underline{\omega}) \frac{\partial \phi(\underline{\omega})}{\partial \beta}. (A2)$$

Using these two results, one can show that

$$\chi_r(\underline{\omega})\frac{\partial \chi_r(\underline{\omega})}{\partial \beta} + \chi_i(\underline{\omega})\frac{\partial \chi_i(\underline{\omega})}{\partial \beta} = I(\underline{\omega})\frac{\partial \ln \chi_m(\underline{\omega})}{\partial \beta} \quad (A3)$$

and

$$\chi_r(\underline{\omega}) \frac{\partial \chi_i(\underline{\omega})}{\partial \beta} - \chi_i(\underline{\omega}) \frac{\partial \chi_r(\underline{\omega})}{\partial \beta} = I(\underline{\omega}) \frac{\partial \phi(\underline{\omega})}{\partial \beta}.$$
 (A4)

This gives us expressions for the derivatives of χ_m and ϕ with respect to β as

$$\frac{\partial \ln \chi_m(\underline{\omega})}{\partial \beta} = \frac{1}{I(\underline{\omega})} \left[\chi_r(\underline{\omega}) \frac{\partial \chi_r(\underline{\omega})}{\partial \beta} + \chi_i(\underline{\omega}) \frac{\partial \chi_i(\underline{\omega})}{\partial \beta} \right], \tag{A5}$$

and

$$\frac{\partial \phi(\underline{\omega})}{\partial \beta} = \frac{1}{I(\underline{\omega})} \left[\chi_r(\underline{\omega}) \frac{\partial \chi_i(\underline{\omega})}{\partial \beta} - \chi_i(\underline{\omega}) \frac{\partial \chi_r(\underline{\omega})}{\partial \beta} \right]. \quad (A6)$$

These equations show how the derivatives for the χ_m and ϕ can be obtained from the directly measured real and imaginary parts of the nonlinear spectrum and their derivatives.

¹D. E. Hare and C. M. Sorensen, "Raman spectroscopic study of dilute HOD in liquid H₂O in the temperature range −31.5 to 160°C," J. Chem. Phys. **93**, 6954–6961 (1990).

²A. Cupane, M. Levantino, and M. G. Santangelo, "Near-infrared spectra of water confined in silica hydrogels in the temperature interval 365-5 K," J. Phys. Chem. B **106**, 11323–11328 (2002).

³S. Šašić, V. H. Segtnan, and Y. Ozaki, "Self-modeling curve resolution study of temperature-dependent near-infrared spectra of water and the investigation of water structure," J. Phys. Chem A 106, 760–766 (2002).

⁴G. E. Walrafen, "Effects of equilibrium H-bond distance and angle changes on Raman intensities from water," J. Chem. Phys. 120, 4868–4876 (2004).

⁵G. E. Walrafen, "New Raman method for aqueous solutions: ζ -function dispersion evidence for strong F⁻-water H-bonds in aqueous CsF and KF solutions," J. Chem. Phys. **123** (2005).

⁶J. D. Smith, C. D. Cappa, K. R. Wilson, B. M. Messer, R. C. Cohen, and R. J. Saykally, "Energetics of hydrogen bond network rearrangements in liquid water," Science 306, 851–853 (2004).

⁷J. D. Smith, C. D. Cappa, K. R. Wilson, R. C. Cohen, P. L. Geissler, and R. J. Saykally, "Unified description of temperature-dependent hydrogen-bond rearrangements in liquid water," Proc. Natl. Acad. Sci. USA 102, 14171–14174 (2005).

⁸I. A. Beta and C. M. Sorensen, "Quantitative information about the hydrogen bond strength in dilute aqueous solutions of methanol from the temperature dependence of the Raman spectra of the decoupled OD stretch," J. Phys. Chem. A **109**, 7850–7853 (2005).

⁹M. Paolantoni, P. Sassi, A. Morresi, and R. S. Cataliotti, "Infrared study of 1-octanol liquid structure," Chem. Phys. 310, 169–178 (2005).

¹⁰S. Sakaguchi, T. Ishiyama, and A. Morita, "Theory and efficient computation of differential vibrational spectra," J. Chem. Phys. 140, 144109 (2014).

¹¹T. Joutsuka and A. Morita, "Improved theory of difference vibrational spectroscopy and application to water," J. Chem. Theory Comp. 12, 5026–5036 (2016).

¹²T. Joutsuka and A. Morita, "Efficient computation of difference vibrational spectra in isothermal-isobaric ensemble," J. Phys. Chem. B **120**, 11229–11238 (2016).

¹³T. Hirano, N. Yazawa, L. Wang, and A. Morita, "Development of efficient computational analysis of difference infrared and Raman spectroscopies," J. Chem. Phys. 157, 124105 (2022).

¹⁴A. G. Ilgen, H. S. Senanayake, W. H. Thompson, and J. A. Greathouse, "Structure and energetics of hydrogen bonding networks in dilute HOD/H2O solutions confined in silica nanopores," Environ. Sci.: Nano 10, 3025–3038 (2023).

¹⁵Z. A. Piskulich and W. H. Thompson, "Temperature dependence of the water infrared spectrum: Driving forces, isosbestic points, and predictions," J. Phys. Chem. Lett. 11, 7762–7768 (2020).

¹⁶A. K. Borkowski and W. H. Thompson, "Shining (infrared) light on the Hofmeister series: Driving forces for changes in the water vibrational spectra in alkali-halide salt solutions," J. Chem. Phys. B **126**, 6700–6712 (2022).

¹⁷Y. Nagata, T. Hasegawa, E. H. Backus, K. Usui, S. Yoshimune, T. Ohto, and M. Bonn, "The surface roughness, but not the water molecular orientation varies with temperature at the water-air interface," Phys. Chem. Chem. Phys. 17, 23559–23564 (2015).

¹⁸M. S. Azam, C. Cai, J. M. Gibbs, E. Tyrode, and D. K. Hore, "Silica surface charge enhancement at elevated temperatures re-

- vealed by interfacial water signals," J. Am. Chem. Soc. **142**, 669–673 (2020).
- ¹⁹C. Cai, M. S. Azam, and D. Hore, "Temperature-dependent chemical functional group reorientation at silicone surfaces," J. Phys. Chem. C **125**, 22214–22222 (2021).
- ²⁰T. Joutsuka and A. Morita, "Electrolyte and temperature effects on third-order susceptibility in sum-frequency generation spectroscopy of aqueous salt solutions," J. Phys. Chem. C 122, 11407–11413 (2018).
- ²¹D. R. Moberg, S. C. Straight, and F. Paesani, "Temperature dependence of the air/water interface revealed by polarization sensitive sum-frequency generation spectroscopy," J. Phys. Chem. B 122, 4356–4365 (2018).
- ²²R. Malik, A. Chandra, B. Das, and A. Chandra, "Theoretical study of the two-dimensional vibrational sum frequency generation spectroscopy of the air—water interface at varying temperature and its connections to the interfacial structure and dynamics," J. Phys. Chem. B 127, 10880–10895 (2023).
- ²³D. Kraemer, M. L. Cowan, A. Paarmann, N. Huse, E. T. Nibbering, T. Elsaesser, and R. J. Dwayne Miller, "Temperature dependence of the two-dimensional infrared spectrum of liquid H₂O," Proc. Natl. Acad. Sci. U. S. A. **105**, 437–442 (2008).
- ²⁴R. A. Nicodemus, K. Ramasesha, S. T. Roberts, and A. Tok-makoff, "Hydrogen bond rearrangements in water probed with temperature-dependent 2D IR," J. Phys. Chem. Lett. 1, 1068–1072 (2010).
- ²⁵R. A. Nicodemus, S. A. Corcelli, J. L. Skinner, and A. Tokmakoff, "Collective hydrogen bond reorganization in water studied with temperature-dependent ultrafast infrared spectroscopy," J. Phys. Chem. B 115, 5604–5616 (2011).
- ²⁶T. Brinzer and S. Garrett-Roe, "Temperature and chain length dependence of ultrafast vibrational dynamics of thiocyanate in alkylimidazolium ionic liquids: A random walk on a rugged energy landscape," J. Chem. Phys. 147, 194501 (2017).
- ²⁷F. Caporaletti, D. Bonn, and S. Woutersen, "Lifetime-associated two-dimensional infrared spectroscopy reveals the hydrogen-bond structure of supercooled water in soft confinement," J. Phys. Chem. Lett., 5951–5956 (2021).
- ²⁸Y. Ni and J. L. Skinner, "Ultrafast pump-probe and 2DIR anisotropy and temperature-dependent dynamics of liquid water within the E3B model," J. Chem. Phys. **141**, 024509 (2014).
- ²⁹D. Ojha and A. Chandra, "Temperature dependence of the ultrafast vibrational echo spectroscopy of OD modes in liquid water from first principles simulations," Phys. Chem. Chem. Phys. 21, 6485–6498 (2019).
- ³⁰A. K. Borkowski, N. I. Campbell, and W. H. Thompson, "Direct calculation of the temperature dependence of 2D-IR spectra. Urea in water," J. Chem. Phys. **158**, 064507 (2023).
- ³¹R. Malik, A. Chandra, B. Das, and A. Chandra, "Temperature dependence of non-Condon effects in two-dimensional vibrational spectroscopy of water," J. Phys. Chem. B 127, 2488–2498 (2023).
- ³²Z. A. Piskulich, D. Laage, and W. H. Thompson, "On the role of hydrogen-bond exchanges in the spectral diffusion of water," J. Chem. Phys. **154**, 064501 (2021).
- ³³S. A. Corcelli, C. P. Lawrence, and J. L. Skinner, "Combined electronic structure/molecular dynamics approach for ultrafast infrared spectroscopy of dilute HOD in liquid H₂O and D₂O," J. Chem. Phys. **120**, 8107–8117 (2004).
- ³⁴S. A. Corcelli and J. L. Skinner, "Infrared and Raman line shapes of dilute HOD in liquid H₂O and D₂O from 10 to 90°C," J. Phys. Chem. A **109**, 6154–6165 (2005).
- ³⁵B. Auer, R. Kumar, J. R. Schmidt, and J. L. Skinner, "Hydrogen bonding and Raman, IR, and 2D-IR spectroscopy of dilute HOD in liquid D₂O," Proc. Natl. Acad. Sci. **104**, 14215–14220 (2007).
- ³⁶S. M. Gruenbaum, C. J. Tainter, L. Shi, and J. L. Skinner, "Robustness of frequency, transition dipole, and coupling maps for water vibrational spectroscopy," J. Chem. Theory Comput. 9, 3109–3117 (2013).

- ³⁷A. Morita and J. T. Hynes, "A theoretical analysis of the sum frequency generation spectrum of the water surface. II. Timedependent approach," J. Phys. Chem. B **106**, 673–685 (2002).
- ³⁸ A. Morita and T. Ishiyama, "Recent progress in theoretical analysis of vibrational sum frequency generation spectroscopy," Phys. Chem. Chem. Phys. **10**, 5801–5816 (2008).
- ³⁹T. L. C. Jansen, S. Saito, J. Jeon, and M. Cho, "Theory of coherent two-dimensional vibrational spectroscopy," J. Chem. Phys. **150**, 100901 (2019).
- ⁴⁰T. Ohto, K. Usui, T. Hasegawa, M. Bonn, and Y. Nagata, "Toward ab initio molecular dynamics modeling for sum-frequency generation spectra; an efficient algorithm based on surface-specific velocity-velocity correlation function," J. Chem. Phys. 143, 124702 (2015).
- ⁴¹N. K. Kaliannan, A. Henao Aristizabal, H. Wiebeler, F. Zysk, T. Ohto, Y. Nagata, and T. D. Kühne, "Impact of intermolecular vibrational coupling effects on the sum-frequency generation spectra of the water/air interface," Mol. Phys. 118, 1620358 (2020).
- ⁴²J. K. Carr, L. E. Buchanan, J. R. Schmidt, M. T. Zanni, and J. L. Skinner, "Structure and dynamics of urea/water mixtures investigated by vibrational spectroscopy and molecular dynamics simulation," J. Phys. Chem. B 117, 13291–13300 (2013).
- $^{43}\mathrm{B.}$ M. Auer and J. L. Skinner, "Vibrational sum-frequency spectroscopy of the liquid/vapor interface for dilute HOD in D₂O," J. Chem. Phys. **129**, 214705 (2008).
- ⁴⁴C. J. Fecko, J. J. Loparo, S. T. Roberts, and A. Tokmakoff, "Local hydrogen bonding dynamics and collective reorganization in water: Ultrafast infrared spectroscopy of HOD/D₂O," J. Chem. Phys. **122**, 054506 (2005).
- ⁴⁵Z. A. Piskulich, O. O. Mesele, and W. H. Thompson, "Activation energies and beyond," J. Phys. Chem. A 123, 7185–7194 (2019).
- ⁴⁶K. J. Tielrooij, C. Petersen, Y. L. Rezus, and H. J. Bakker, "Reorientation of HDO in liquid H₂O at different temperatures: Comparison of first and second order correlation functions," Chem. Phys. Lett. **471**, 71–74 (2009).
- ⁴⁷J. R. Schmidt, S. A. Corcelli, and J. L. Skinner, "Pronounced non-Condon effects in the ultrafast infrared spectroscopy of water," J. Chem. Phys. **123**, 044513 (2005).
- ⁴⁸S. M. Gruenbaum, P. A. Pieniazek, and J. L. Skinner, "Vibrational spectroscopy of water in hydrated lipid multi-bilayers. II. Two-dimensional infrared and peak shift observables within different theoretical approximations," J. Chem. Phys. 135, 164506 (2011).
- ⁴⁹The LAMMPS molecular dynamics package, http://lammps.sandia.gov (downloaded July 8, 2020).
- ⁵⁰S. Plimpton, "Fast parallel algorithms for short-range molecular dynamics," J. Comput. Phys. 117, 1–19 (1995).
- ⁵¹H. J. C. Berendsen, J. R. Grigera, and T. P. Straatsma, "The missing term in effective pair potentials," J. Phys. Chem. 91, 6269–6271 (1987).
- ⁵²Z. A. Piskulich, O. O. Mesele, and W. H. Thompson, "Removing the barrier to the calculation of activation energies: Diffusion coefficients and reorientation times in liquid water," J. Chem. Phys. **147**, 134103 (2017).
- ⁵³S. Nosé, "A molecular dynamics method for simulations in the canonical ensemble," Mol. Phys. **52**, 255–268 (1984).
- ⁵⁴W. G. Hoover, "Canonical dynamics: Equilibrium phase-space distributions," Phys. Rev. A 31, 1695–1697 (1985).
- ⁵⁵D. P. Shoemaker, C. W. Garland, and J. W. Nibler, Experiments in Physical Chemistry (McGraw-Hill, New York, 1989).
- ⁵⁶E. A. Raymond, T. L. Tarbuck, M. G. Brown, and G. L. Richmond, "Hydrogen-bonding interactions at the vapor/water interface investigated by vibrational sum-frequency spectroscopy of HOD/H₂O/D₂O mixtures and molecular dynamics simulations," J. Phys. Chem. B **107**, 546–556 (2003).
- ⁵⁷H. J. Bakker and J. L. Skinner, "Vibrational spectroscopy as a probe of structure and dynamics in liquid water," Chem. Rev. 110, 1498–1517 (2010).